

Clustering and Triaxial Deformations of ^{40}Ca

Yasutaka Taniguchi,^{1,2} Masaaki Kimura,³ Yoshiko Kanada-En'yo,² and Hisashi Horiuchi⁴

¹*Department of Physics, Kyoto University, Kyoto 606-8502, Japan*

²*Yukawa Institute for Theoretical Physics, Kyoto University, Kyoto 606-8502, Japan*

³*Institute of Physics, University of Tsukuba, Tsukuba 305-8571, Japan*

⁴*Research Center of Nuclear Physics, Osaka University, Ibaraki 567-0047, Japan*

(Dated: November 20, 2018)

We have studied the positive-parity states of ^{40}Ca using antisymmetrized molecular dynamics (AMD) and the generator coordinate method (GCM). Imposing two different kinds of constraints on the variational calculation, we have found various kinds of ^{40}Ca structures such as a deformed-shell structure, as well as α - ^{36}Ar and ^{12}C - ^{28}Si cluster structures. After the GCM calculation, we obtained a normal-deformed band and a superdeformed band together with their side bands associated with triaxial deformation. The calculated $B(E2)$ values agreed well with empirical data. It was also found that the normal-deformed and superdeformed bands have a non-negligible α - ^{36}Ar cluster component and ^{12}C - ^{28}Si cluster component, respectively. This leads to the presence of an α - ^{36}Ar higher-nodal band occurring above the normal-deformed band.

PACS numbers: 21.60.-n, 23.20.-g

I. INTRODUCTION

Nuclear dynamics possess various aspects depending on mass regions, excitation energies, and so on. In light-weight nuclei, it is known that clustering plays a significant role in the features of ground and excited states [1, 2]. On the other hand, in heavier nuclei, the clustering effects are not clear, though many theoretical [3, 4] and experimental [5] studies have been conducted. In the fp -shell region, the focus should be on proton-rich $N \sim Z$ nuclei, because such nuclei can have a clustered structure comprising stable nucleus. Moreover, proton-rich nuclei have a large radius and stronger Coulomb repulsion, and may also derive a cluster structure. In the scope of this research, the features of cluster structures in ^{40}Ca are a key issue, because they are the heaviest $N = Z$ stable nuclei, and many experimental data exist for this nuclei. In this paper, we have studied the structure of ^{40}Ca as a starting point to understand the structures of medium- and heavy-weight $N \sim Z$ nuclei. ^{40}Ca has a typical double closed-shell structure nucleus and has a spherical ground state. However, it is known that many kinds of deformed band appear in low energy regions. The first $K^\pi = 0^+$ band built on the $J^\pi = 0_2^+$ state (3.35 MeV) is considered to be a normal-deformed (ND) state and the dominant configuration is $4p$ - $4h$ [6]. The $K^\pi = 2^+$ band built on $J^\pi = 2_2^+$ (5.25 MeV) exists just above the $K^\pi = 0^+$ band. It has been suggested that the ND band deforms triaxially and has the $K^\pi = 2^+$ side band due to triaxiality [7, 8].

The α - ^{36}Ar cluster structure has been studied for a long time, because ^{40}Ca is an analogue of ^{16}O , which has an α - ^{12}C cluster structure in the first $K^\pi = 0^+$ band, as a double closed-shell nuclei. The local potential model [9, 10, 11] and α - ^{36}Ar orthogonal condition model (OCM) [12, 13] have been performed theoretically. Ohkubo *et al.* suggested that the first $K^\pi = 0^+$ band (ND) has an α - ^{36}Ar structure, and predicted that its parity-doublet

$K^\pi = 0^-$ band and α - ^{36}Ar higher nodal band exist in highly excited states [10]. Sakuda *et al.* obtained the $K^\pi = 2^+$ band as well as the $K^\pi = 0^+$ and 0^- states using the α - ^{36}Ar OCM, and succeeded in reproducing $E2$ transition strengths [13]. Experimentally, the α - ^{36}Ar structure is studied through the $^{36}\text{Ar}(^6\text{Li},d)^{40}\text{Ca}$ reaction [14, 15]. The states in these $K^\pi = 0^+$ and 0^- bands are populated by the α -transfer reactions and have large α spectroscopic factors [14]. In the experiments we describe, the α - ^{36}Ar higher-nodal states were also observed [15].

It has been suggested that the states in the $K^\pi = 0^+$ rotational band built on the $J^\pi = 0_3^+$ state (5.21 MeV) have a $8p$ - $8h$ configuration [7], and have been observed during experimental work searching for the $8p$ - $8h$ states with $^{32}\text{S}(^{12}\text{C}, \alpha)^{40}\text{Ca}$ reactions [16]. Due to the strong population in the multi-nucleon transfer data and the strong $E2$ transitions [17], the 0^+ (5.21 MeV), 2^+ (5.63 MeV) and 4^+ (6.54 MeV) bands have been thought to belong to the superdeformed (SD) band with the dominant $8p$ - $8h$ configuration. Recently, by using GAMMA-SPHERE array detectors, the level structure of the deformed bands in ^{40}Ca has been explored and many excited states up to high spin have been discovered. This band was thus confirmed as the SD band [18].

Motivated by these the experimental observations, many theoretical microscopic studies on deformed states of ^{40}Ca have been performed recently with the methods of Skyrme-Hartree-Fock (SHF) [19], SHF-BCS + GCM [20], spherical-basis AMD [21] and the shell model [22]. Inakura *et al.* performed cranked SHF calculations without assuming axial symmetry, though energy levels were not calculated [19]. Bender *et al.* performed SHF-BCS + GCM calculations [20]. Although they calculated energy levels and quadrupole transition strengths in the ND and SD bands, they could not study triaxiality nor side bands because they assumed axial symmetry. In these studies, the relationship between deformed states and clus-

ter structure was not discussed. It has been suggested that the SD state forms a ^{12}C - ^{28}Si -like cluster structure in spherical-basis AMD [21]. Within the spherical-basis AMD, triaxiality does not appear in ND nor SD states.

The purpose of the present study is to understand the clustering and triaxial deformations in the low energy states of ^{40}Ca in a unified manner. We use the framework of AMD + GCM. The basis functions of GCM are obtained by energy variation after parity projection with constraints. We adopted two kinds of constraints. One is a constraint on the quadrupole deformation parameter β (β -constraint) and the other is on the distance d between clusters' centers of mass (d -constraint). It has already been proven that the d -constraint is useful for obtaining various kinds of clustering wave function, which are not computed within a simple β -constraint [23]. For example, the $^8\text{Be}(2\alpha)$ - ^{12}C cluster structure in ^{20}Ne is calculated with a d -constraint but not with the β -constraint. Also in the case of ^{40}Ca , many kinds of cluster structure, for example α - ^{36}Ar , $^8\text{Be}(2\alpha)$ - ^{32}S and ^{12}C - ^{28}Si , can be calculated with the d -constraint, although no cluster structure is obtained in ^{40}Ca with the β -constraint. We superposed mean-field-type and cluster-type wave functions calculated with β - and d -constraints respectively, and calculated energies and $E2$ transition strength. We analyzed the superposed wave functions in order to investigate clustering and triaxial deformations.

This paper is organized as follows. In the next section (§II), we explain the framework of this study. The calculated results and discussions are presented in §III, and lastly, we present a summary in §IV.

II. FRAMEWORK

A. Wave Function and Hamiltonian

We used the theoretical framework of AMD + GCM. In the present study, the AMD wave function is a Slater determinant of triaxially deformed Gaussian wave packets (deformed-basis AMD),

$$|\Phi_{\text{int}}\rangle = \hat{\mathcal{A}}|\varphi_1, \varphi_2, \dots, \varphi_A\rangle, \quad (1a)$$

$$|\varphi_i\rangle = |\phi_i, \chi_i, \tau_i\rangle, \quad (1b)$$

$$\langle \mathbf{r} | \phi_i \rangle = \prod_{\sigma=x,y,z} \left(\frac{2\nu_\sigma}{\pi} \right)^{\frac{1}{4}} \exp \left[-\nu_\sigma \left(r_\sigma - \frac{Z_{i\sigma}}{\sqrt{\nu_\sigma}} \right)^2 \right], \quad (1c)$$

$$|\chi_i\rangle = \alpha_i |\uparrow\rangle + \beta_i |\downarrow\rangle, \quad (1d)$$

$$|\tau_i\rangle = |p\rangle \text{ or } |n\rangle. \quad (1e)$$

Here, the complex parameters \mathbf{Z}_i , which represent the centroids of the Gaussian in phase space, take independent values for each single particle wave function. The width parameters ν_x , ν_y and ν_z are real parameters and take independent values for each of the x -, y - and z -directions, but are common for all nucleons. The spin

part $|\chi_i\rangle$ is parametrized by α_i and β_i and the isospin part $|\tau_i\rangle$ is fixed as $|p\rangle$ (proton) or $|n\rangle$ (neutron). The quantities $(\mathbf{Z}_i, \alpha_i, \beta_i, \nu_x, \nu_y, \nu_z)$ are variational parameters and are optimized by energy variation as explained in the next subsection.

The trial wave function in the energy variation with constraints is a parity-projected wave function,

$$|\Phi^\pi\rangle = \frac{1 + \pi \hat{P}_r}{2} |\Phi_{\text{int}}\rangle, \quad (2)$$

where π is parity and \hat{P}_r is the parity operator. In this study, we will discuss positive parity states.

The Hamiltonian is,

$$\hat{H} = \hat{K} + \hat{V}_N + \hat{V}_C - \hat{K}_G, \quad (3)$$

where \hat{K} and \hat{K}_G are the kinetic energy and the energy of the center of mass motion respectively, and \hat{V}_N is the effective nucleon-nucleon interaction. We have used Gogny D1S force (D1S) and Skyrme SLy7 force (SLy7) in the present work. The Coulomb force \hat{V}_C is approximated by a sum of seven Gaussians.

B. Energy Variation, Angular Momentum Projection and the Generator Coordinate Method

We performed energy variation and optimized the variational parameters included in the trial wave function (Eqs. (1)) to find the state that minimizes the energy of the system E^π ,

$$E^\pi = \frac{\langle \Phi^\pi | \hat{H} | \Phi^\pi \rangle}{\langle \Phi^\pi | \Phi^\pi \rangle} + V_{\text{cnst}}. \quad (4)$$

Here, we add the constraint potential V_{cnst} to the expectation value of Hamiltonian \hat{H} in order to obtain the minimum energy state under the optional constraint condition. In this study, we employed two types of constraint, which are on the quadrupole deformation parameter β (β -constraint) and the distance between clusters' centers of mass, d (d -constraint) by employing the potential V_{cnst} ,

$$V_{\text{cnst}} = \begin{cases} v_{\text{cnst}}^\beta (\beta - \tilde{\beta})^2 & \text{for } \beta\text{-constraint,} \\ v_{\text{cnst}}^d (d_{C_m-C_n} - \tilde{d}_{C_m-C_n})^2 & \text{for } d\text{-constraint.} \end{cases} \quad (5)$$

Here β is the matter quadrupole deformation parameter, which is defined in Ref. 24, and $d_{C_m-C_n}$ is the distance between the clusters' centers of mass C_m and C_n ,

$$d_{C_m-C_n} = |\mathbf{R}_m - \mathbf{R}_n|, \quad (6)$$

$$R_{n\sigma} = \frac{1}{A_n} \sum_{i \in C_n} \frac{\text{Re} Z_{i\sigma}}{\sqrt{\nu_\sigma}}, \quad (7)$$

where A_n is the mass number of cluster C_n and the expression $i \in C_n$ means that the i th nucleon is contained in

cluster C_n . It should be noted that the σ ($= x, y, z$) component of the spatial center of the single-particle wave function $|\varphi_i\rangle$ is $\frac{\text{Re}Z_{i\sigma}}{\sqrt{\nu_\sigma}}$. When sufficiently large values are chosen for v_{cnst}^β and v_{cnst}^d , the resultant values β and $d_{C_m-C_n}$ of energy variation become $\tilde{\beta}$, $\tilde{d}_{C_m-C_n}$, respectively. We constrained the $d_{\alpha-36\text{Ar}}$ and $d_{12\text{C}-28\text{Si}}$ values for the d -constraint. In each calculation of energy variation, we constrained one of β , $d_{\alpha-36\text{Ar}}$ and $d_{12\text{C}-28\text{Si}}$. A detailed explanation regarding the d -constraint may be found in Ref. 23.

The energy variation with the AMD wave function is carried out using the frictional cooling method [25]. The time evolution equation for the complex parameters \mathbf{Z}_i , α_i and β_i is

$$\frac{dX_i}{dt} = -\mu_X \frac{\partial E^\pi}{\partial X_i^*}, \quad (i = 1, 2, \dots, A), \quad (8)$$

where X_i is \mathbf{Z}_i , α_i or β_i , and that for the real parameters ν_x, ν_y and ν_z is

$$\frac{d\nu_\sigma}{dt} = -\mu_\nu \frac{\partial E^\pi}{\partial \nu_\sigma}, \quad (\sigma = x, y, z). \quad (9)$$

The quantities μ_X and μ_ν are arbitrary positive real numbers. The energy of the system decreases as time progresses, and after a sufficient number of time steps, we obtain the minimum energy state.

After the constrained energy variation for $|\Phi^\pi\rangle$, we superposed the optimized wave functions employing the quadrupole deformation parameter β and the distances between the centers of mass among clusters $d_{C_m-C_n}$ for C_m-C_n configurations as the generator coordinate,

$$|\Phi_M^{J^\pi}\rangle = \sum_K \hat{P}_{MK}^{J^\pi} \left(\sum_i f_{iK}^\beta |\Phi_i^\beta\rangle + \sum_{i, C_m-C_n} f_{iK}^{d_{C_m-C_n}} |\Phi_i^{d_{C_m-C_n}}\rangle \right) \quad (10)$$

where $\hat{P}_{MK}^{J^\pi}$ is the parity and total angular momentum projection (AMP) operator, and $|\Phi_i^\beta\rangle$ and $|\Phi_i^{d_{C_m-C_n}}\rangle$ are optimized wave functions with β - and $d_{C_m-C_n}$ -constraints for the constrained values $\tilde{\beta}^{(i)}$ and $\tilde{d}_{C_m-C_n}^{(i)}$ respectively. The integrals over the three Euler angles included in $\hat{P}_{MK}^{J^\pi}$ are evaluated by numerical integration. The coefficients f_{iK}^β and $f_{iK}^{d_{C_m-C_n}}$ are determined by the Hill-Wheeler equation,

$$\delta \left(\langle \Phi_M^{J^\pi} | \hat{H} | \Phi_M^{J^\pi} \rangle - \epsilon \langle \Phi_M^{J^\pi} | \Phi_M^{J^\pi} \rangle \right) = 0. \quad (11)$$

C. Squared Overlap

We defined squared overlap SO to estimate the overlap of a specific model space in the superposed wave

TABLE I: Expectation values of kinetic and potential energies around the ground state, ND and SD minima. K , V_{NN} , V_{LS} and V_{C} denote kinetic energy, central, spin-orbit and Coulomb potentials.

interaction	β	total	K	V_{NN}	V_{LS}	V_{C}
Gogny D1S	0.00	-340.9	634.2	-1046.2	-0.1	71.2
Skyrme SLy7	0.00	-340.7	637.9	-1050.0	-0.0	71.5
Gogny D1S	0.39	-326.7	654.6	-1033.7	-18.4	70.9
Skyrme SLy7	0.39	-326.8	653.7	-1031.9	-19.4	70.8
Gogny D1S	0.62	-322.2	670.9	-1029.9	-33.6	70.4
Skyrme SLy7	0.61	-322.3	676.2	-1035.9	-33.3	70.7

function. Suppose the non-orthonormalized wave functions $|\Phi_i^X\rangle$ span the functional space $\{X\}$, for example, $\{X\} = \{|\Phi_i^\beta\rangle\}$, $\{|\Phi_i^{d_{\alpha-36\text{Ar}}}\rangle\}$ or $\{|\Phi_i^{d_{12\text{C}-28\text{Si}}}\rangle\}$. Orthonormalized wave functions $|\tilde{\Phi}_\alpha^X\rangle$ are obtained by performing unitary transformations from $|\Phi_i^X\rangle$,

$$|\tilde{\Phi}_\alpha^X\rangle = u_{\alpha i} |\Phi_i^X\rangle, \quad (12a)$$

$$\langle \tilde{\Phi}_\alpha^X | \tilde{\Phi}_\beta^X \rangle = \delta_{\alpha\beta}. \quad (12b)$$

Using the $|\tilde{\Phi}_\alpha^X\rangle$, squared overlap between $|\Phi\rangle$ and the functional space $\{X\}$, SO is defined as

$$SO = \sum_\alpha |\langle \tilde{\Phi}_\alpha^X | \Phi \rangle|^2. \quad (13)$$

III. RESULTS AND DISCUSSIONS

A. Various Structures Obtained with β - and d -constraints

We performed the energy variation after the projection to the positive-parity state imposing two different kinds of constraints, β - and d -constraints.

Figure 1 (a) shows the obtained energy curves as a function of matter quadrupole deformation β . By applying the β -constraint we obtained energy curves for D1S (solid line) and SLy7 (dotted line). Both forces give quite similar curves that have three local minima or shoulders at $\beta \sim 0, 0.4$ and 0.6 . As shown in Table. I, they also give approximately the same kinetic and potential energies around each minimum. Therefore, we mainly discuss the D1S result and make some comments on the differences between D1S and SLy7 below. The lowest minimum at $\beta=0$ corresponds to the spherical ground state and the two minima at $\beta \sim 0.4$ and 0.6 correspond to the ND and SD states respectively. The excitation energies of the ND and SD minima are approximately 14 MeV and 18 MeV. This result qualitatively agrees with the constrained SHF calculation using SLy4 [19]. On the other hand, the energy curve in the constrained SHF-BCS calculation with SLy6 [20] reveals different behavior. It does not have the ND minimum nor shoulder, but has a SD minimum. The excitation energy of the SD minimum

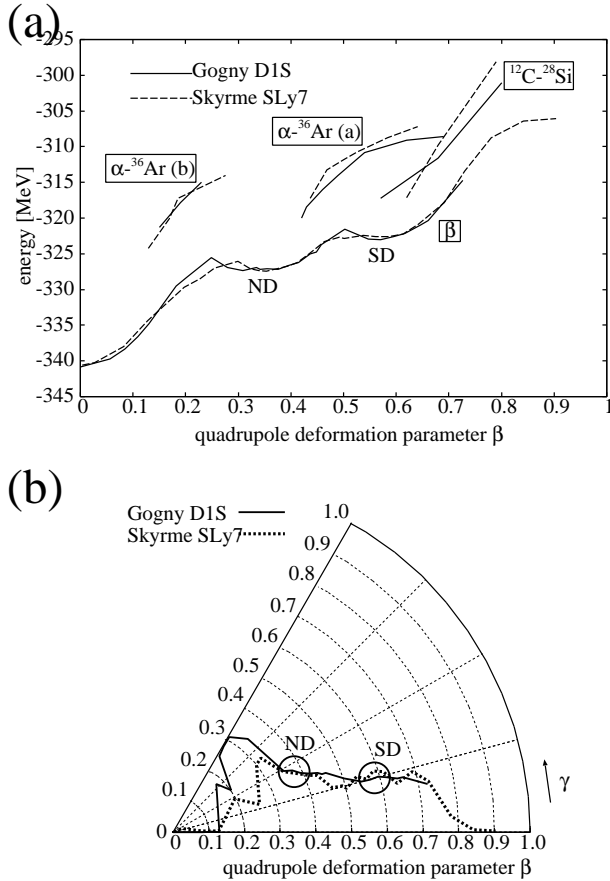


FIG. 1: (a): The energy curves for the positive-parity states obtained using β -, $d_{\alpha\text{-}^{36}\text{Ar}}$ - and $d_{^{12}\text{C}\text{-}^{28}\text{Si}}$ -constraints. The energies are plotted as functions of quadrupole deformation β . The solid (dotted) line shows the results for D1S (SLy7). (b): Projection of the energy curves onto the β - γ plane. The solid (dotted) line shows the results for D1S (SLy7).

is much smaller than ours and that of Ref. 19. This difference may be due to the strong pairing correlation reported in Ref. 20.

In the present calculation, we do not make any assumptions regarding the spatial symmetry of the wave function nor put any constraints on the quadrupole deformation γ . γ therefore has the optimal value for each given value of β . Figure 1 (b) shows the projection of the energy curve onto the β - γ plane. It shows that in most regions the system is triaxially deformed and the degree of the triaxial deformation greatly changes as a function of β . Starting from the spherical ground state, the system rapidly changes to oblate deformation around $\beta=0.15\text{-}0.25$ via a small prolate deformation. Then, it changes to triaxial deformation around $\beta=0.35$ where the ND minimum appears and the system has the largest triaxiality. With a further increase of β , γ decreases gradually from $\gamma=30^\circ$ at $\beta=0.35$ to $\gamma=15^\circ$ at $\beta=0.70$. The SD minimum that appears at $\beta=0.60$ also has a large triaxial deformation $\gamma=15^\circ$.

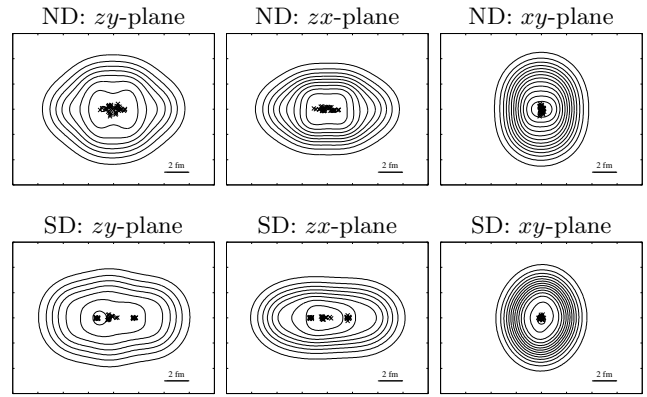


FIG. 2: Density distributions of the ND and SD minima obtained using the β -constraint. The crosses in the figure show the centroids of the wave packets. The deformation parameters are $(\beta, \gamma) = (0.39, 25.2^\circ)$ and $(0.62, 14.5^\circ)$ for the ND and SD minima, respectively.

The deformation of the β - γ curve for SLy7 shows similar behavior except in the region of $\beta=0.15\text{-}0.30$. In the $\beta \sim 0.30$ region, the deformation obtained for SLy7 is triaxial, which is different from the oblate deformation with D1S. The wave functions in this region did not affect the ND and SD bands, nor their side bands as shown later.

Figure 2 shows the density distribution of the ND and SD minima, and confirms their large triaxial deformation. It also reveals the deformed mean-field nature of the ND minimum and implies the existence of a relationship between the SD minimum and the cluster structure. At the limit when all $\mathbf{Z}_i \rightarrow \mathbf{0}$ (all centroids of single particle wave packets go to the origin of the coordinate frame), the AMD wave function is identical to an eigenstate of the deformed harmonic oscillator whose oscillation number is given by the relation $\omega_\sigma = 2\hbar\nu_\sigma/M$. In contrast, when the system has a cluster-like structure, the \mathbf{Z}_i are separated into several groups to describe cluster subunits. In the case of the ND minimum, the centroids of the single particle wave packets are located around the origin and the wave packets are strongly deformed, $(\nu_x, \nu_y, \nu_z) = (0.16, 0.14, 0.11)$, suggesting that the nature of the mean-field is deformed. In the case of the SD minimum, the wave packets are further deformed, $(\nu_x, \nu_y, \nu_z) = (0.17, 0.15, 0.10)$, and reveal the aspect of a triaxially deformed mean-field. In the case of the SD minimum, the centroids of the single particle wave packets appear separated into two (28+12) or three ((12+16)+12) groups and the density distribution reveals an octupole deformation implying that the SD minimum also has an asymmetric cluster-like nature. It will be shown using the d -constraint that this has a significant overlap with the $^{12}\text{C}\text{-}^{28}\text{Si}$ cluster structure.

There are few studies on the triaxial deformation of ^{40}Ca , but some theoretical work has suggested the triaxiality of the ND [7, 8] and SD [19] states. The present calculation with the β -constraint has shown that most

of the states on the energy curve have a triaxial deformation. We therefore consider it indispensable to study the issue without the assumption of spatial symmetry in order to understand the excited states of ^{40}Ca .

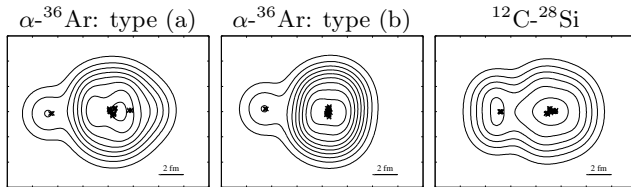


FIG. 3: Density distributions of intrinsic states obtained with the d -constraint. $d_{\alpha-^{36}\text{Ar}}$ is fixed to 5.0 fm for $\alpha-^{36}\text{Ar}$ (a) and (b). $d_{^{12}\text{C}-^{28}\text{Si}}$ is fixed to 4.0 fm for $^{12}\text{C}-^{28}\text{Si}$. The crosses in the figure show the centroids of the wave packets.

With the β -constraint, we do not find spatially developed clustering at the ND and SD minima, although the density distribution of the SD state implies its relationship to clustering. We have therefore applied the d -constraint. We discuss the results obtained with $d_{\alpha-^{36}\text{Ar}}$ - and $d_{^{12}\text{C}-^{28}\text{Si}}$ -constraints. Other combinations of clusters such as $2\alpha-^{32}\text{Si}$ have been also applied, but they have appeared at comparatively high excitation energy levels and were not involved with the ND and SD states even after the GCM calculation.

By applying the $d_{\alpha-^{36}\text{Ar}}$ -constraint, we have obtained an excited energy curve above the energy curve obtained with the β -constraint (Fig. 1). Two different kinds of structure appeared on the energy curve. In both cases, the system has well developed $\alpha-^{36}\text{Ar}$ cluster structures as may be clearly seen in their density distributions (Fig. 3 (a) and (b)). The difference between them is the orientation of the axis of symmetry in the oblately deformed ^{36}Ar cluster. The first is denoted as type (a). In this type, the axis of symmetry for ^{36}Ar is perpendicular to the vector that connects the α and ^{36}Ar clusters. Therefore the whole system has a triaxial deformation. This type of structure is favored under $d_{\alpha-^{36}\text{Ar}}$ -constraints with large $d_{\alpha-^{36}\text{Ar}}$ values and appears in the region of $\beta = 0.45-0.7$. The second kind of structure is denoted type (b). In this type, the axis of symmetry in the ^{36}Ar cluster is parallel to the vector that connects the α and ^{36}Ar clusters, resulting in an axial deformation of the system. This type is obtained when the inter-cluster distance is restricted to a shorter distance ($d_{\alpha-^{36}\text{Ar}}=4.5-5.5$ fm) and appears in the region of $\beta=0.15-0.3$. It is interesting that type (b) is bound deeper than type (a) for shorter inter-cluster distances and ^{36}Ar changes its orientation as the inter-cluster distance becomes larger. We assume that ^{36}Ar changes its orientation to make the overlap and potential energy between the α and ^{36}Ar clusters larger.

By applying a $d_{^{12}\text{C}-^{28}\text{Si}}$ -constraint ($d_{^{12}\text{C}-^{28}\text{Si}}=4.0-6.0$ fm), we obtained a strongly deformed and excited energy curve that appears in the region of $\beta=0.55-0.8$. The system has a prominent $^{12}\text{C}-^{28}\text{Si}$ cluster structure and is triaxially deformed as shown in Fig. 3. In this case, we

did not find a change in the orientation of the clusters.

d -constraints have generated excited energy curves in which the system has prominent cluster structures. The fact that these wave functions are mixed with the wave functions obtained with the β -constraint and play an important role in describing highly excited bands is discussed below.

B. Angular Momentum Projection

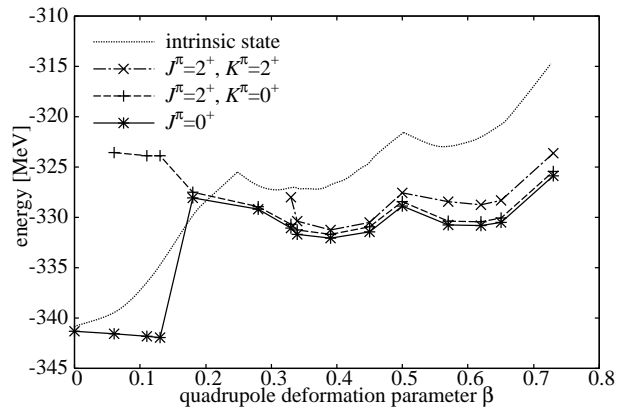


FIG. 4: The energy curves of the $J^\pi = 0^+$ and 2^+ states projected from wave functions obtained with the β -constraint with D1S.

The wave functions obtained above are projected onto the eigenstate of the total angular momentum. The $J^\pi=0^+$ and 2^+ states obtained with the β -constraint are shown in Fig. 4. AMP reduces the excitation energies of the deformed states. For example, the $J^\pi=0^+$ states of ND and SD are lowered by approximately 6 and 9 MeV respectively. As a result, they almost degenerate in terms of energy. We have obtained two 2^+ states for each given value of β in the deformed region by the diagonalization of the quantum number K . These states are denoted as $K^\pi=0^+$ and 2^+ according to the dominant component of their wave function. The presence of the $K^\pi=2^+$ state is due to the triaxial deformation in the $\beta \gtrsim 0.3$ region. As will be discussed below, the triaxial deformations of the ND and SD states leads to the presence of their side bands, $K^\pi=2^+$.

The energy of the wave functions obtained with the d -constraint are also lowered by AMP. The $\alpha-^{36}\text{Ar}$ type (a), (b) and $^{12}\text{C}-^{28}\text{Si}$ states are lowered by approximately 5-10, 10-15 MeV and 10 MeV respectively. $\alpha-^{36}\text{Ar}$ type (a) and $^{12}\text{C}-^{28}\text{Si}$ wave functions have the $K^\pi=2^+$ components because of the triaxial deformation.

C. GCM Calculation

1. Energy levels and deformations

After applying the AMP, we carried out GCM calculations. For the GCM basis, we adopted 15 β -constrained wave functions $\beta = 0.00$ - 0.73 , 7 $d_{\alpha^{-36}\text{Ar}}$ -constrained wave functions of type (a) with $d_{\alpha^{-36}\text{Ar}} = 4.5$ - 9.0 fm, 3 $d_{\alpha^{-36}\text{Ar}}$ -constrained wave functions of type (b) with $d_{\alpha^{-36}\text{Ar}} = 4.5$ - 5.5 fm, and 3 $d_{^{12}\text{C}-^{28}\text{Si}}$ -constrained wave functions with $d_{^{12}\text{C}-^{28}\text{Si}} = 4.0$ - 6.0 fm. Then we obtained the final GCM wave functions by diagonalizing Hamiltonian and norm matrices for the parity and angular momentum projected states with $K^\pi = 0^+$ and $\pm 2^+$ for the 28 independent wave functions.

The theoretical energy levels of the GCM states and the experimental levels are shown in Fig. 5. The energies of the simple AMP for the main components in the band heads are also given. In most levels, the GCM states gain 1-2 MeV from the simple AMP. Experimentally, the $K^\pi = 0^+$, 2^+ and 0^+ bands built on $J^\pi = 0_2^+$, 2_1^+ and 0_3^+ states are known to be the ND band ($K^\pi = 0_{\text{ND}}^+$), the side band of the ND band ($K^\pi = 2_{\text{ND}}^+$) and the SD band ($K^\pi = 0_{\text{SD}}^+$). In the result of the GCM calculation, we obtained three $K^\pi = 0^+$ and two $K^\pi = 2^+$ bands in low-lying states above the ground state. We assigned the first and second $K^\pi = 0^+$ bands to the observed $K^\pi = 0_{\text{ND}}^+$ and 0_{SD}^+ bands respectively, and the first $K^\pi = 2^+$ band to the observed $K^\pi = 2_{\text{ND}}^+$ band, because the theoretical moments of inertia and electric transition strength $B(E2)$ of these bands correlate well with the experimental data for the corresponding bands as discussed below. The second $K^\pi = 2^+$ band in the results is regarded as the side band $K^\pi = 2_{\text{SD}}^+$ of the SD band. We denote the third theoretical $K^\pi = 0^+$ band as the $K^\pi = 0_{\text{ob}}^+$ band because of the oblate shape. We also obtained the $K^\pi = 0^+$ and 2^+ bands in highly excited states with large $\alpha^{-36}\text{Ar}$ cluster structure components, which are the candidates for $\alpha^{-36}\text{Ar}$ higher-nodal bands, $K^\pi = 0_{\text{hn}}^+$ and 2_{hn}^+ , observed experimentally [15].

Let us consider the GCM results of the low-lying states (ground, ND, SD and oblate states) in more detail by analyzing the squared overlap between $J^\pi = 0^+$ states and the AMP states from the β -constrained wave functions. The ND state's $K^\pi = 0_{\text{ND}}^+$ and 2_{ND}^+ bands are mainly constructed from the β -constrained wave functions around the ND minimum occurring in the $\beta \sim 0.4$ region. Their band-head states have a maximum overlap of approximately 85% for the triaxially deformed state with $(\beta, \gamma) = (0.39, 25.2^\circ)$. There is no mixing between the ND state and the ground state. The squared overlap with the β -constrained wave functions is almost unchanged up to high spin states along the $K^\pi = 0_{\text{ND}}^+$ band. On the other hand, in the $K^\pi = 2_{\text{ND}}^+$ band, the squared overlap of each component changes with the increase in spin, which implies the change of structure in this band. In the result of the GCM calculation, the theoretical ex-

TABLE II: The squared overlap (SO) of β -constrained wave functions and d -constrained wave functions.

	K^π	J^π	β -constraint	d -constraint	
			SO	SO	
ND	0_{ND}^+	0^+	0.99	0.37	$\alpha^{-36}\text{Ar}$
		2^+	0.99	0.40	
		4^+	0.99	0.40	
	2_{ND}^+	2^+	0.99	0.40	
		3^+	0.99	0.45	
		4^+	0.99	0.46	
SD	0_{SD}^+	0^+	0.95	0.59	$^{12}\text{C}-^{28}\text{Si}$
		2^+	0.95	0.59	
		4^+	0.95	0.56	
	2_{SD}^+	2^+	0.95	0.61	
		3^+	0.95	0.61	
		4^+	0.95	0.60	
$\alpha^{-36}\text{Ar}$ higher-nodal	0_{hn}^+	0^+	0.41	0.49	$\alpha^{-36}\text{Ar}$
		2^+	0.45	0.50	
		4^+	0.52	0.50	
	2_{hn}^+	2^+	0.38	0.55	
		3^+	0.52	0.45	
		4^+	0.59	0.39	

citation energies of the band heads in the $K^\pi = 0_{\text{ND}}^+$ and 2_{ND}^+ bands are 11.2 MeV and 12.1 MeV respectively. These are much higher than the experimental excitation energies. However, the rotational energies in the band are reproduced well, as shown in Fig. 6.

The SD states, $K^\pi = 0_{\text{SD}}^+$ and 2_{SD}^+ , are constructed mainly by β -constrained wave functions around the SD local minimum. The main component is the β -constrained wave function with triaxial shape, $(\beta, \gamma) = (0.62, 14.5^\circ)$. The squared overlap is more than 90% in the band-head states, and almost unchanged up to high spin states along the $K^\pi = 0_{\text{SD}}^+$ and 2_{SD}^+ bands. A small degree of mixing between the ND and SD bands is seen in the $\beta \sim 0.5$ region. The result of the GCM calculation reveals the band-head energies of the $K^\pi = 0_{\text{SD}}^+$ and 2_{SD}^+ bands are 12.1 MeV and 14.0 MeV respectively. Although the present calculations overestimate the experimental excitation energies of the $K^\pi = 0_{\text{SD}}^+$ band as well as the ND bands, the rotational energies in the band are reproduced well as shown in Fig. 6.

The oblate bands are dominated by the β -constrained wave functions in the $\beta \sim 0.3$ region. The main component is the oblate wave function with $(\beta, \gamma) = (0.33, 51.2^\circ)$. The oblate band ($K^\pi = 0_{\text{ob}}^+$) has not been discovered experimentally yet. Our prediction of the oblate band is consistent with spherical-basis AMD [21] as well as SHF calculations [19].

2. Cluster components

In this section we discuss the contribution of the cluster wave functions in the ND and SD states. In Table II, we

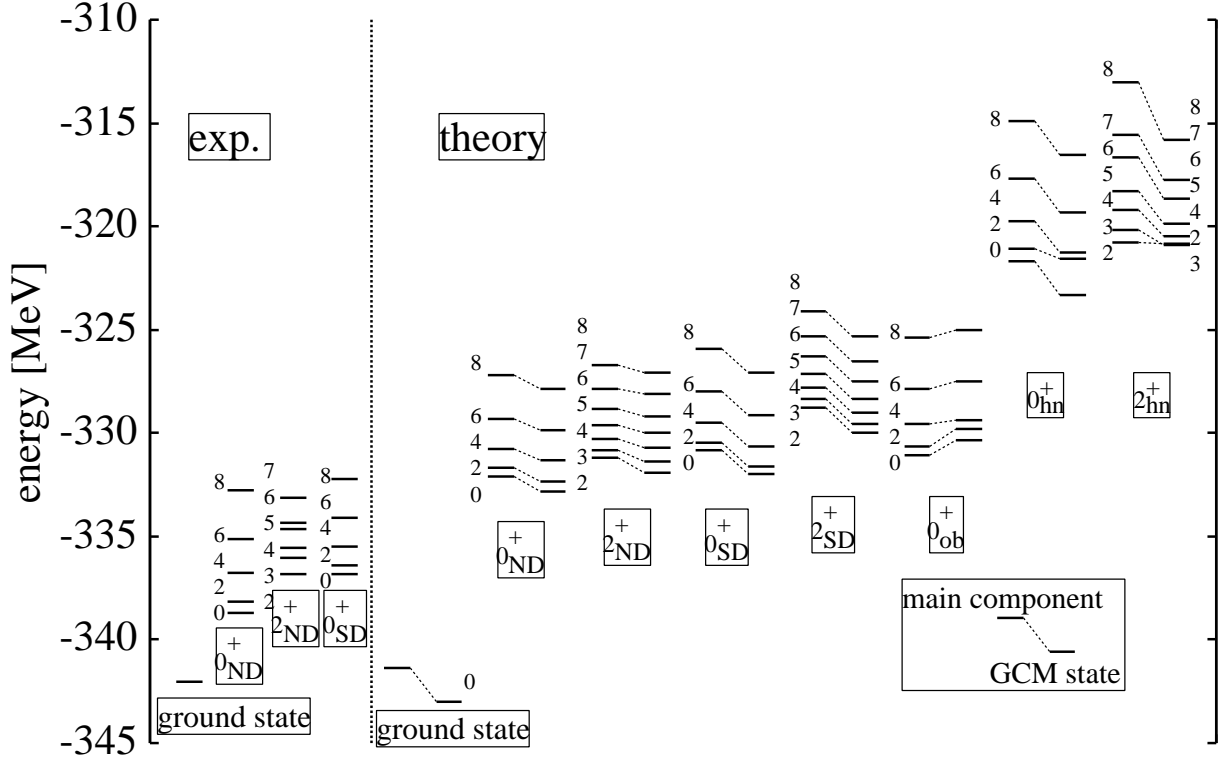


FIG. 5: Energy levels in ^{40}Ca . The left hand side represents experimental values, and the right hand side theoretical values. The energies of superposed wave functions and that of the main component are represented.

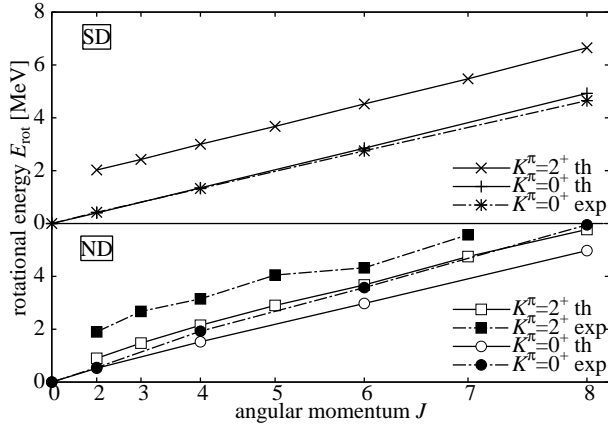


FIG. 6: The rotational energies $E_{\text{rot}} \equiv E - E_{0^+}$ of the ND and SD bands as functions of the angular momentum $J(J+1)$.

list the squared overlap (SO) values of the GCM states with the α - ^{36}Ar configuration space given by the set of $d_{\alpha-^{36}\text{Ar}}$ -constrained wave functions, and those with the ^{12}C - ^{28}Si configuration space, as well as the SO values for the model space of the β -constrained wave functions. The definition of the specific functional space is explained in §II C. The squared overlap between the ND state and β -

constrained wave functions is 99%. This means that the ND state is practically represented by the β -constrained wave functions alone. On the other hand, it is surprising that the ND states have a significant overlap of approximately 40% with the $d_{\alpha-^{36}\text{Ar}}$ -constrained wave functions as well. This indicates that the β -constrained wave functions for the ND states include the α - ^{36}Ar component, though the spatially developed cluster structure is not seen in the density distributions. The α - ^{36}Ar cluster component in the ND band is mainly consistent with type (a) wave functions, while the squared overlap of type (b) wave functions in ND states is almost negligible. The result, that the ND state contains an α - ^{36}Ar cluster structure component, is associated with the results of the α - ^{36}Ar potential model calculation [10, 11], $^{36}\text{Ar}(^6\text{Li}, d)^{40}\text{Ca}$ reaction [14, 15] and α - ^{36}Ar OCM calculation [13].

The SD states are dominated by the β -constrained wave function as well as the ND states. However, the SD states also have a large overlap with the $d_{^{12}\text{C}-^{28}\text{Si}}$ -constrained wave functions as reflected by the SO of approximately 60%. We found that the β -constrained AMD wave functions for the SD states also include the cluster components, even though the cluster structure is not visible in the density distributions. The ^{12}C - ^{28}Si cluster configurations also make a significant contribution to the energy of the SD states. In particular, the energies of the SD states gain 1-2 MeV due to the mixing of ^{12}C -

^{28}Si cluster structure wave functions. This is associated with the results of spherical-basis AMD [21] according to which the SD states have a ^{12}C - ^{28}Si cluster structure configuration.

3. α - ^{36}Ar higher-nodal states, $K^\pi = 0_{\text{hn}}^+$ and 2_{hn}^+ bands

As shown in Fig. 5, we obtained $K^\pi = 0^+$ and 2^+ bands with large α - ^{36}Ar cluster components in the excitation energy region approximately 10 MeV higher than the ND band. The main component of the higher α - ^{36}Ar bands, $K^\pi = 0_{\text{hn}}^+$ and 2_{hn}^+ , are d_{α - $^{36}\text{Ar}}$ -constrained wave functions obtained with a large distance d_{α - $^{36}\text{Ar}} = 6.0$ fm. We assume that this corresponds to the α - ^{36}Ar higher-nodal band observed with the $^{36}\text{Ar}(^6\text{Li},d)^{40}\text{Ca}$ reaction [15], where the fragments of the $J^\pi = 0^+$ state for this band were reported around 8 MeV above the band-head of the ND band.

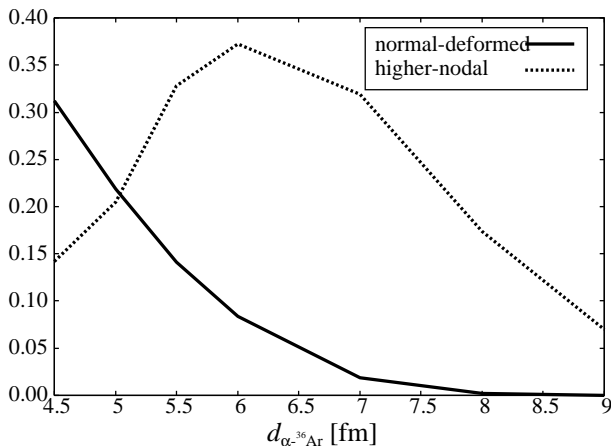


FIG. 7: The squared overlap of the $J^\pi = 0^+$ states in the ND band ($K^\pi = 0_{\text{ND}}^+$) and the α - ^{36}Ar higher-nodal band ($K^\pi = 0_{\text{hn}}^+$) with d_{α - $^{36}\text{Ar}}$ -constrained wave functions.

The squared overlap between d_{α - $^{36}\text{Ar}}$ -constrained wave functions and the $J^\pi = 0^+$ states in $K^\pi = 0_{\text{ND}}^+$ and 0_{hn}^+ bands are shown in Fig. 7. The squared overlap for 0_{hn}^+ is suppressed in the small d_{α - $^{36}\text{Ar}}$ region and has a peak at d_{α - $^{36}\text{Ar}} = 6$ fm, which demonstrates the nodal property of the inter-cluster motion in this band. It can be assumed that the α - ^{36}Ar higher-nodal states arise from the inter-cluster excitation built on the ND states. In other words, the significant component of the α - ^{36}Ar cluster structure in the ND states must be essential for the formation of the higher-nodal states, because the cluster component in the small distance region is possible if the ND states contain no cluster component. This means that the higher-nodal states appear as a consequence of the orthogonality to the cluster components with a small distance d , which are already contained in the ND states. This situation is similar to the relationship between the ground band and

TABLE III: Theoretical and experimental $B(E2)$ of ^{40}Ca . The units of transitions are Weisskopf units, $B(E2)_{\text{W.u.}} = 8.12 e^2\text{fm}^4$. The asterisk-marked experimental $B(E2)$ values are taken from Ref. 13, and other values are taken from Ref. 26.

$K_i^\pi \rightarrow K_f^\pi$	I_i	I_f	$B(E2)_{\text{th}}$	$B(E2)_{\text{exp}}$
$0_{\text{ND}}^+ \rightarrow \text{g. s.}$	2^+	0^+	< 0.05	2.26 ± 0.14
$2_{\text{ND}}^+ \rightarrow \text{g. s.}$	2^+	0^+	< 0.05	0.13 ± 0.04
$0_{\text{SD}}^+ \rightarrow \text{g. s.}$	2^+	0^+	< 0.05	0.20 ± 0.05
$0_{\text{ND}}^+ \rightarrow 0_{\text{ND}}^+$	2^+	0^+	39.0	32 ± 4
	4^+	2^+	55.5	61 ± 10
	6^+	4^+	63.7	17_{-17}^{+9}
	8^+	6^+	65.1	—
$0_{\text{SD}}^+ \rightarrow 0_{\text{SD}}^+$	2^+	0^+	118.5	—
	4^+	2^+	166.0	170 ± 40
	6^+	4^+	178.8	—
	8^+	6^+	145.2	—
$2_{\text{ND}}^+ \rightarrow 2_{\text{ND}}^+$	3^+	2^+	66.6	$> 71, 82 \pm 26^*$
	4^+	2^+	22.0	$23 \pm 5^*$
	4^+	3^+	23.6	$< 1300^*$
$2_{\text{ND}}^+ \rightarrow 0_{\text{ND}}^+$	2^+	0^+	< 0.05	$1.3 \pm 0.4, 0.54 \pm 0.14^*$
	2^+	2^+	44.0	$22 \pm 6, 25 \pm 6^*$
	3^+	2^+	0.1	$3.7 \pm 0.7^*$
	3^+	4^+	23.3	$< 22^*$
	4^+	2^+	0.3	3.8 ± 0.8
	4^+	4^+	14.7	$6.8 \pm 5.2^*$
	6^+	4^+	< 0.05	4.2 ± 1.0
$0_{\text{SD}}^+ \rightarrow 0_{\text{ND}}^+$	0^+	2^+	0.1	17 ± 3
	2^+	0^+	< 0.05	2.6 ± 0.7
	4^+	2^+	< 0.05	2.6 ± 0.6
$0_{\text{SD}}^+ \rightarrow 2_{\text{ND}}^+$	4^+	2^+	0.2	22 ± 6

α - ^{40}Ca higher-nodal band in ^{44}Ti suggested by Kimura *et al.* with deformed-basis AMD [28].

4. Electric transitions

Here, we investigate the electric quadrupole strengths and discuss the band structure. The theoretical and experimental values of $E2$ transition strengths $B(E2)$ are shown in Fig. 8. The $B(E2)$ values for intra-band transitions are remarkably strong, and the transitions between the $K^\pi = 0_{\text{ND}}^+$ and $K^\pi = 2_{\text{ND}}^+$ bands, and those between the $K^\pi = 0_{\text{SD}}^+$ and 2_{SD}^+ bands are also strong. This reflects the side-band features of the $K^\pi = 2_{\text{ND}}^+$ and $K^\pi = 2_{\text{SD}}^+$ bands, corresponding to $K^\pi = 0_{\text{ND}}^+$ and $K^\pi = 0_{\text{SD}}^+$ respectively. The inter-band transitions between ND and SD states and those from ND or SD states to the ground state are underestimated. This is because mixing of wave functions among these bands is small in our calculation. On the other hand, we predict the transitions from the oblate $K^\pi = 0_{\text{ob}}^+$ band to the ND bands, $K^\pi = 0_{\text{ND}}^+$ and 2_{ND}^+ , because of the mixing among these bands.

Detailed comparisons between the theoretical values

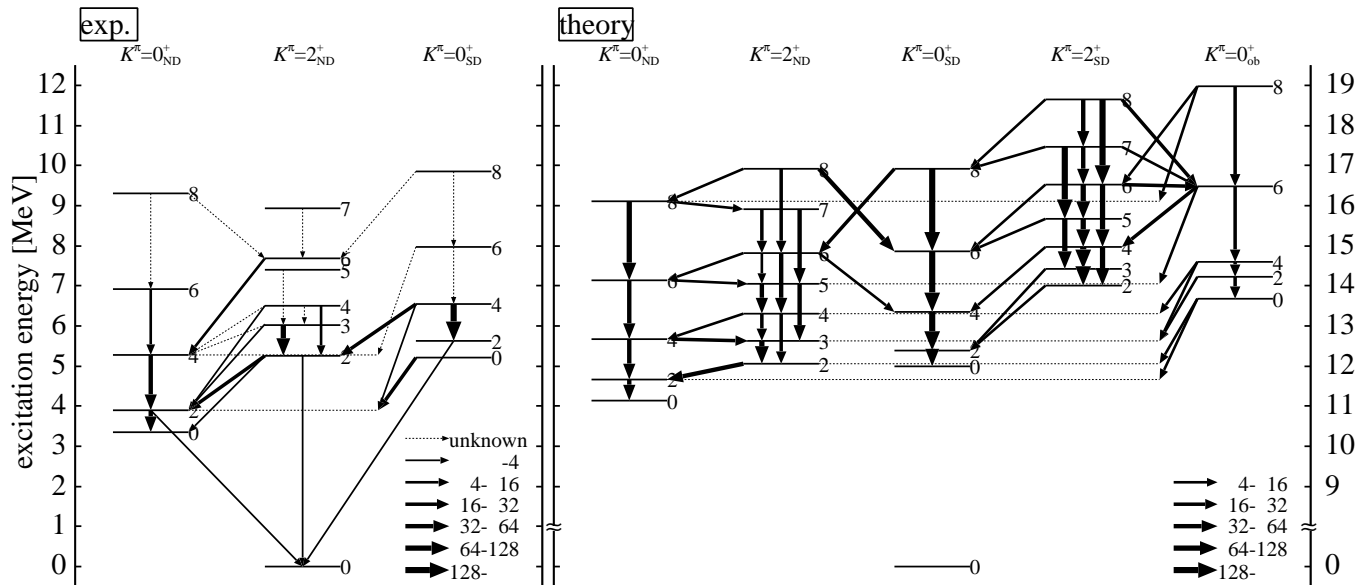


FIG. 8: Experimental and theoretical $B(E2)$ values. Units are Weisskopf units, $B(E2)_{\text{W.u.}} = 8.12 e^2 \text{fm}^4$ for ^{40}Ca . In theoretical values, transitions stronger than $4.4 B(E2)_{\text{W.u.}}$ are presented. The experimental data are taken from Refs. 13 and 26. “unknown” indicates the transition has been observed but $B(E2)$ has not been measured.

and experimental data of the $B(E2)$ values are shown in Table III. The $B(E2)$ values for the intra-band transitions in the ND and SD states are reproduced well, except for the $6^+ \rightarrow 4^+$ transition when $K^\pi = 0^+_{\text{ND}}$. The small value of the experimental $B(E2; 6^+ \rightarrow 4^+)$ is overestimated by the calculation, although the error in the experimental value is rather large.

Quadrupole moment

The theoretical and experimental values of quadrupole moments deduced from the $E2$ strengths for the $K^\pi = 0^+_{\text{ND}}$, 2^+_{ND} and 0^+_{SD} bands are listed in Table IV. The results of other theoretical studies are also shown in the table. The intrinsic quadrupole moment Q is defined by the $B(E2)$ value as follows.

$$Q \equiv \sqrt{\frac{16\pi B(E2, I_i \rightarrow I_f)}{5e^2 \langle I_i K 2 0 | I_f K \rangle^2}}, \quad (14)$$

where $\langle I_i K 2 0 | I_f K \rangle$ is the Clebsch-Gordan coefficient.

The theoretical quadrupole moments of the ND and SD states are around 130 fm^2 and 220 fm^2 respectively. The values are almost unchanged up to high spin. This means that the ND and SD bands consist of approximately rigid rotor states. These results are consistent with the rigid rotor-like spin dependence of the excitation energies of the ND and SD states shown in Fig. 6. The theoretical Q moments are consistent with experimental values evaluated from life-time measurements and branching ratios (I) except for the $6^+ \rightarrow 4^+$ transition in the ND state. The small value of the experimental Q moment for the

$6^+ \rightarrow 4^+$ transition might suggest some structure change in high spin states in the ND band.

We compared our results with those of other theoretical studies. The Q values in (4) α - ^{36}Ar OCM are consistent with the present values for the ND states. This may indicate that the deformation of the ND states in our calculations is similar to that calculated with the α - ^{36}Ar cluster model. In (1) the spherical-basis AMD and (3) the shell model, smaller Q values for the $K^\pi = 0^+$ states were obtained by comparison to our model. In (2) SHF-BCS + GCM, the Q values are also smaller than our results for $K^\pi = 0^+$ states. In particular, the Q moments for the $4^+ \rightarrow 2^+$ transition in both the ND and SD states are remarkably small. This shows that the ND and SD bands obtained in the SHF-BCS + GCM calculation are not rigid rotor-like. This seems to be inconsistent with experimental results regarding the rigid rotor-like property, which has been found in rotational energies and $E2$ transitions. In recent experimental observations, the Q values have been obtained by globally fitting all transitions. They ((II)-a and b) are smaller than the values of the life-time measurement (I) and also smaller than the present results. Further analysis requires more detailed measurements of the $E2$ transition strengths.

Triaxial rotor

In this section we discuss the characteristics of the side bands, $K^\pi = 2^+$, in the ND and SD states. In a naive collective model, a $K^\pi = 2^+$ band can be described by either a triaxial rotor or a γ vibration. In order to identify the mode of the side bands, it is useful to analyze the

TABLE IV: Intrinsic quadrupole moments of the ND band and the SD band extracted from $B(E2)$. For theoretical study, (1), (2), (3) and (4) are taken from the results of spherical-basis AMD [21], HFB-BCS + GCM [20], shell model [22] and α - ^{36}Ar OCM [13], respectively. For experimental data, (I) is obtained from life-time and branching ratio, asterisk-marked values are taken from Ref. 13 and others are from Ref. 26. (II)-a and (II)-b are taken from Refs. 18 and 27 respectively, which are obtained through a global fitting of all the transitions.

K^π		theory				experiment			
I_i	I_f	present work	(1)	(2)	(3)	(4)	(I)	(II)-a	(II)-b
0_{ND}^+			A3					band 2	
2^+	0^+	126.2	57	75.2	121	117	110 ± 10		74 ± 14
4^+	2^+	125.9	64	23.9	118	117	130 ± 10		74 ± 14
6^+	4^+	128.5	64	77.4	105	117	66^{+16}_{-66}		74 ± 14
8^+	6^+	127.0	78		83	115			74 ± 14
2_{ND}^+									
3^+	2^+	123.4				119	$140 \pm 20^*$		
4^+	2^+	122.7			106	115	$120 \pm 10^*$		
4^+	3^+	85.1				115	$< 630^*$		
0_{SD}^+			A3 (A2)					band 1	band 1
2^+	0^+	219.9	129	133.9	171		180^{+39}_{-29}	130 ± 5	
4^+	2^+	217.8	129	97.6	169		220 ± 26	180^{+39}_{-29}	130 ± 5
6^+	4^+	215.3	121	160.2	167		180^{+39}_{-29}	130 ± 5	
8^+	6^+	189.7	97 (70)	157.9	166		180^{+39}_{-29}	130 ± 5	

ratio of $E2$ strength for $K^\pi = 2^+$ to $K^\pi = 0^+$ transitions,

$$R = \frac{B(E2; (2^+, K^\pi = 2^+) \rightarrow (0^+, K^\pi = 0^+))}{B(E2; (2^+, K^\pi = 2^+) \rightarrow (2^+, K^\pi = 0^+))}, \quad (15)$$

where $B(E2; (J_i^\pi, K_i^\pi) \rightarrow (J_f^\pi, K_f^\pi))$ is the value of quadrupole electric transition strength from a J_i^π state in the K_i^π band to a J_f^π state in the K_f^π band. The R value is set to the constant value 7/10 in the γ vibration mode, while it is a function of the static γ parameter in the triaxial rotor mode [29],

$$R^{\text{rot}}(\gamma) = \frac{7}{20} \left[1 - \frac{3 - 2 \sin^2(3\gamma)}{\sqrt{9 - 8 \sin^2(3\gamma)}} \right] \bigg/ \frac{\sin^2(3\gamma)}{9 - 8 \sin^2(3\gamma)}. \quad (16)$$

The function $R^{\text{rot}}(\gamma)$ is plotted as a function of γ value in Fig. 9. The value of R^{rot} is 0.7 for the axial symmetric limit, $\gamma \rightarrow 0^\circ$ and 60° . As the triaxiality increases, R^{rot} decreases, going to zero at the peak of triaxiality, $\gamma = 30^\circ$. Regarding the ND state, the theoretical value R of the $E2$ strength ratio is nearly equal to 0, and the experimental value $R = 0.06$ is also close to 0. Both the values agree well with $R^{\text{rot}}(\gamma \sim 30^\circ)$ but are far from that of the γ vibration limit, 0.7. In the present results, the γ value of the main component of the ND state is 25.2° , which is consistent with $\gamma \sim 30^\circ$ for the triaxial rotor derived from the experimental R value. We therefore conclude that the mode of the observed $K^\pi = 2_{\text{ND}}^+$ band is a triaxial rotor, not a γ vibration.

Regarding the SD state, the theoretical value of R is equal to 0.51, and the γ value of the main component of the theoretical SD state is 14.5° . These values, $(\gamma, R) = (14.5^\circ, 0.51)$ can be described by the relation $R^{\text{rot}}(\gamma)$ in Eq. (15) for the triaxial rotor. This indicates

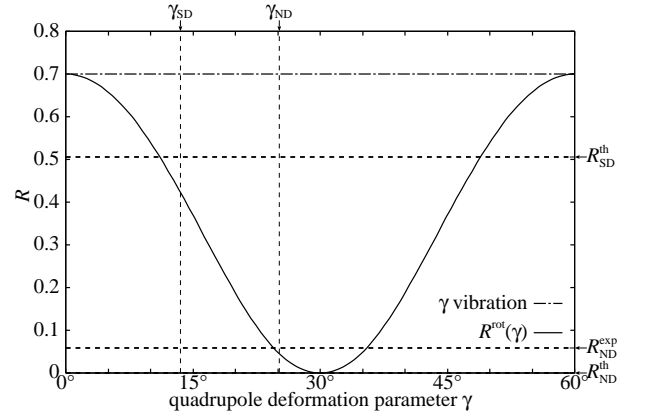


FIG. 9: The values of the ratio of $E2$ strength R as a function of γ value. The dot-dashed line and the solid line show the limiting values of the γ -vibration and the triaxial rotor respectively. The $R_{\text{ND}}^{\text{th}}(\sim 0)$ and $R_{\text{SD}}^{\text{th}}(= 0.51)$ values are the theoretical R values for the ND and SD states derived from the $E2$ transition strengths respectively, while $R_{\text{ND}}^{\text{exp}}$ is that of the experiment for the ND state. The deformation parameters $\gamma_{\text{ND}}(= 25.2^\circ)$ and $\gamma_{\text{SD}}(= 14.5^\circ)$ for the main components of the ND and SD states are also shown.

that the case of $K^\pi = 2_{\text{SD}}^+$ in the SD state is the side band of the triaxial rotor. The $K^\pi = 2_{\text{SD}}^+$ band has not yet been observed experimentally. In order to confirm the triaxiality of the SD band, observations of the $K^\pi = 2_{\text{SD}}^+$ band and the $E2$ strength for the inter-band transitions are required.

IV. SUMMARY

We investigated the ground state and excited states of ^{40}Ca in the framework of deformed-basis AMD focusing on the aspects of triaxiality and clustering in the deformed states. Superposing mean-field-type and cluster structure-type wave functions obtained with β - and d -constraints respectively, we obtained the ground states, ND, SD, oblate and α - ^{36}Ar higher-nodal states. We found both the ND and SD bands are constructed from triaxially deformed shapes, and we obtained the $K^\pi = 2^+$ side bands of these bands. The theoretical $B(E2)$ and moments of inertia are consistent with experimental data, although the excitation energies are higher than empirical values. By analyzing quadrupole moments calculated from the $B(E2)$ and the $E2$ strength ratio R values, we found that the ND and SD states can be understood by a relatively rigid rotor conception of triaxial deformations. The ND band and its side band contain approximately 40% of the α - ^{36}Ar cluster structure component, and the SD band and its side band con-

tain approximately 60% of the ^{12}C - ^{28}Si cluster structure component. The α - ^{36}Ar higher-nodal band was obtained due to the excitation of inter-cluster motion between the α and ^{36}Ar clusters. The present results suggested that cluster correlation will be important for deformation and excitation even in medium- and heavy-weight nuclei.

Acknowledgments

This work has been supported by JSPS Research Fellowships for Young Scientists. The numerical calculations were carried out on SX8 at YITP in Kyoto University and on SX5 and SX8 at RCNP in Osaka University. The authors would like to thank Dr. Inakura and Dr. Fujiwara for fruitful discussions. This work is supported by a Grant-in-Aid for the 21st Century COE ‘‘Center for Diversity and Universality in Physics’’ from the Ministry of Education, Culture, Sports, Science and Technology of Japan (MEXT).

-
- [1] H. Horiuchi, K. Ikeda and Y. Suzuki, Prog. Theor. Phys. Suppl. No. 52, 89 (1972), and references therein.
 - [2] Y. Fujiwara, H. Horiuchi, K. Ikeda, M. Kamimura, K. Katō, Y. Suzuki and E. Uegaki, Prog. Theor. Phys. Suppl. No. 68, 29 (1980), and references therein.
 - [3] F. Michel, S. Ohkubo and G. Reidemeister, Prog. Theor. Phys. Suppl. No. 132, 7 (1998), and references therein.
 - [4] T. Sakuda and S. Ohkubo, Prog. Theor. Phys. Suppl. No. 132, 103 (1998), and references therein.
 - [5] T. Yamaya, K. Katori, M. Fujiwara, S. Kato and S. Ohkubo, Prog. Theor. Phys. Supp., No. 132, 73 (1998), and references therein.
 - [6] W. J. Gerace and A. M. Green, Nucl. Phys. **93**, 110 (1967).
 - [7] W. J. Gerace and A. M. Green, Nucl. Phys. **A123**, 241 (1969).
 - [8] W. J. Gerace and J. P. Mestre, Nucl. Phys. **A285**, 253 (1977).
 - [9] K. F. Pal and R. G. Lovas, Phys. Lett. **B96**, 19 (1980).
 - [10] S. Ohkubo and K. Umehara, Prog. Theor. Phys. **80**, 598 (1988).
 - [11] G. Reidemeister, S. Ohkubo and F. Michel, Phys. Rev. **C41**, 63 (1990).
 - [12] T. Ogawa, Y. Suzuki and K. Ikeda, prog. Theor. Phys. **57**, 1072 (1977).
 - [13] T. Sakuda and S. Ohkubo, Phys. Rev. **C49**, 149 (1994).
 - [14] T. Yamaya, M. Saito, M. Fujiwara, T. Itahashi, K. Katori, T. Suehiro, S. Kato, S. Hatori and S. Ohkubo, Phys. Lett. **B306**, 1 (1993).
 - [15] T. Yamaya, M. Saitoh, M. Fujiwara, T. Itahashi, K. Katori, T. Suehiro, S. Kato, S. Hatori and S. Ohkubo, Nucl. Phys. **A573**, 154 (1994).
 - [16] R. Middleton, J. D. Garrett and H. T. Fortune, Phys. Lett. **B39**, 339 (1972).
 - [17] J. R. MacDonald, D. H. Wilkinson and D. E. Alburger, Phys. Rev. **C3**, 219 (1971), and references therein.
 - [18] E. Ideguchi *et al.*, Phys. Rev. Lett. **87**, 222501 (2001).
 - [19] T. Inakura, S. Mizutori, M. Yamagami and K. Matsuyanagi, Nucl. Phys. **A710**, 261 (2002).
 - [20] M. Bender, H. Flocard and P. -H. Heenen. Phys. Rev. **C68**, 044321 (2003).
 - [21] Y. Kanada-En’yo and M. Kimura, Phys. Rev. **C72**, 064322 (2005).
 - [22] E. Caurier, J. Menendez, F. Nowacki, A. Poves, Phys. Rev. **C75**, 054317 (2007).
 - [23] Y. Taniguchi, M. Kimura and H. Horiuchi, Prog. Theor. Phys. **112**, 475 (2004).
 - [24] A. Dote, H. Horiuchi and Y. Kanada-En’yo, Phys. Rev. **C56**, 1844 (1997).
 - [25] Y. Kanada-Enyo and H. Horiuchi, Prog. Theor. Phys. **93**, 115 (1995).
 - [26] J. A. Cameron and B. Singh, Nuclear Data Sheets 102, 293 (2004).
 - [27] C. Chiara *et al.*, Phys. Rev. **C67**, 041303 (2003).
 - [28] M. Kimura, H. Horiuchi, Nucl. Phys. **A767**, 58 (2006).
 - [29] A. S. Davydov and G. F. Filippov, Nucl. Phys. **8**, 237 (1958).